# Statistics of Nonlinear Internal Waves during the Shallow Water 2006 Experiment

MOHSEN BADIEY AND LIN WAN

*College of Earth, Ocean, and Environment, University of Delaware, Newark, Delaware*

JAMES F. LYNCH

*Applied Ocean Physics and Engineering, Woods Hole Oceanographic Institution, Woods Hole, Massachusetts*

(Manuscript received 3 November 2015, in final form 12 February 2016)

ABSTRACT

During the Shallow Water Acoustic Experiment 2006 (SW06) conducted on the New Jersey continental shelf in the summer of 2006, detailed measurements of the ocean environment were made along a fixed reference track that was parallel to the continental shelf. The time-varying environment induced by nonlinear internal waves (NLIWs) was recorded by an array of moored thermistor chains and by X-band radars from the attending research vessels. Using a mapping technique, the three-dimensional (3D) temperature field for over a month of NLIW events is reconstructed and analyzed to provide a statistical summary of important NLIW parameters, such as the NLIW propagation speed, direction, and amplitude. The results in this paper can be used as a database for studying the NLIW generation, propagation, and fidelity of nonlinear internal wave models.

## 1. Introduction

In the last three decades, many nonlinear internal wave (NLIW) events have been observed in the Mid-Atlantic Bight using satellites (Sawyer 1983), space shuttle photographs (Zheng et al. 1993), and in situ measurements (Shroyer et al. 2011). A statistical analysis of 34 internal waves spotted in a space shuttle picture in 1993 has been reported by Zheng et al. In Zheng et al.'s paper, they showed the spatial distribution of these events using two specific geotimes. While their report contained valuable statistical information of the NLIW on the New Jersey continental shelf, their results were temporally undersampled.

The particular dataset (M. Badiey 2006, unpublished data) examined in this paper comes from the Shallow Water Acoustic Experiment 2006 (SW06) conducted in the Mid-Atlantic Bight near the continental shelf break directly offshore from Atlantic City, New Jersey. During the SW06, one very specific measurement aimed at quantifying and understanding the NLIWs was the so-called thermistor farm, a logarithmically spaced array of 18 thermistor strings that imaged a substantial portion of an NLIW train as it propagated through the farm. Another type of NLIW observations in SW06 is the surface imaging from ship-based X-band radar. The two research vessels (i.e., *Oceanus* and *Sharp*) tracked the leading NLIW front as the NLIW packet propagated toward the shoreline. In the SW06, the fixed geometry of sensors was designed where the dynamic behavior of the water column could be measured continuously as a function of time but the spatial dimension was undersampled. To fully capture both spatial and temporal domains, an interpolating model of the water column was developed where the three-dimensional data can be reconstructed using existing measured data points in geotimes (Badiey et al. 2013).

While the oceanography of the generation and propagation of NLIW waves in SW06 has been reported in the past (Moum and Nash 2008; Shroyer et al. 2009, 2011), here we present statistical values of 30 internal

Supplemental information related to this paper is available at the Journals Online website: http://dx.doi.org/10.1175/JTECH-D-15-0221.s1.

*Corresponding author address*: Mohsen Badiey, College of Earth, Ocean, and Environment, University of Delaware, 111 Robinson Hall, Newark, DE 19716.
E-mail: badiey@udel.edu

DOI: 10.1175/JTECH-D-15-0221.1

wave events observed from 3 to 31 August 2006 during SW06. Section 2 of this paper gives a historical parameterization of the NLIW in shallow water (Apel et al. 2007) followed by the NLIW field measurements. Section 3 presents the statistical values. Section 4 is a summary of the presented results.

## 2. NLIW measurements during SW06

More details about SW06 can be found in Newhall et al. (2007). Figure 1a is the satellite picture of internal wave packets on 13 August 2006 showing various NLIW front features partially covering the SW06 experimental setup. The dots are various sensors and the yellow box is the thermistor farm. In distilling our internal wave field measurements for use in a simple parameterized model, we will follow the lead of John Apel (Apel et al. 2007), who proposed a two-layer ocean model of the nonlinear internal waves. Two-layer and three-layer models are the most common simplified NLIW descriptors, and the two-layer models adopted here have far more theoretical literature available describing their properties. Top and side views of Apel's scheme are shown in Figs. 1b,d, respectively, and the parameters are enumerated in Table 1, along with their units and typical scales. Top and side views of the SW06 interpolated temperature data inside the thermistor farm at a specific geotime (2236:00 UTC 17 August 2006) are also shown in Figs. 1c,e corresponding to Figs. 1b,d, respectively. The interpolated data are obtained by a three-dimensional mapping technique for evolving internal waves (Badiey et al. 2013).

As one example of our analysis, we present the propagation of an NLIW packet from 0422:30 to 0650:30 UTC 14 August 2006. Movie 1 (supplemental material file JTECH-D-15-022s1) shows dynamics of this event. We explain the movie by showing the layout of a single frame at 0613:00 UTC. Figure 2a shows the top view of the reconstructed internal wave fronts (i.e., gray curves) approaching a fixed reference track (red line) at a speed of 0.68 m s$^{-1}$. The R/V *Sharp* stationed at a point (green dot) right of the reference line recorded the surface radar expression of the NLIW passage [see inset (Fig. 2b)]. Figures 2c–j show various elements of data collection. Vertical temperature profiles at three thermistor chains (45, 32, and 54) are shown in Figs. 2c–e, respectively. The vertical dashed–dotted lines indicate the reference time of this figure at 0613:00 UTC 14 August 2006. The sound speed profiles at three points—54 (blue), 32 (red), and 45 (black)—are shown in Fig. 2f. The vertical cross section of the temperature field within the thermistor farm is shown in Fig. 2g. The horizontal cross section of the interpolated temperature data (24 m below sea surface) at three ocean patches is shown in Figs. 2h–j. The arrows represent the directions of NLIW propagation at each patch with respect to true north. We have successfully reconstructed 30 of more than 80 internal wave events from 3 to 31 August 2006. Many of the events with small first-layer depth ($H_1$) could not be reconstructed due to the failure of the temperature sensors deployed at about 1 m below the sea surface (Newhall et al. 2007). The internal wave fronts in Fig. 2a are obtained by matching the internal wave (IW) propagation at the three ocean patches (Figs. 2h–j). As an independent measurement to verify the interpolation method explained here, the internal wave fronts during the propagation were recorded in the footprint of the R/V *Sharp* radar. To get a good resolution, we started recording the surface manifestation of the waves on the radar every 30 s when the leading edge first appeared. The locations of the several leading wave fronts on the radar coincide with the interpolation results (black curves). The locations of sensors deployed along the reference track are shown as the numbered yellow dots in these subplots and are listed in Table 2. For brevity, only the latitude and longitude coordinates of the sensors in boldface are given in this table. The rest of the coordinates for each group can be obtained from Figs. 2a,h–j. The dynamic behavior of the passing NLIW is clearly depicted when the movie is played. The advancing NLIW front and the approach of the NLIW packet toward the fixed track (red line), and the 3D water column changes are shown.

The ADCP data were also collected to obtain the current speed at various locations along the reference track. An example of the processed ADCP data measured at point 30 during the aforementioned NLIW event is presented in Fig. 3, which shows the east–west component of the current speed (Fig. 3a), the north–south component (Fig. 3b), and the up–down (vertical) component (Fig. 3c). Figure 3d is the temperature profile measured at the same point for the same time period. The magnitude and direction of current change drastically in concert with the soliton depression, especially the upward (red) and downward (blue) currents, which occur each time a soliton passes by (Fig. 3c). The vertical current–induced circulation interacts with the sea surface that causes radar backscatter, shown in Fig. 2b (Ramos et al. 2009).

## 3. Statistical results

Using the tools shown in section 2, we have developed a statistical database from 30 recorded NLIW events during SW06. These statistical data were obtained when the NLIW packet was located inside the thermistor farm, such that the first front was close to the far edge of the farm (i.e., along points 4–7 shown for an event on 17 August 2006 in Fig. 1c). There are eight directly

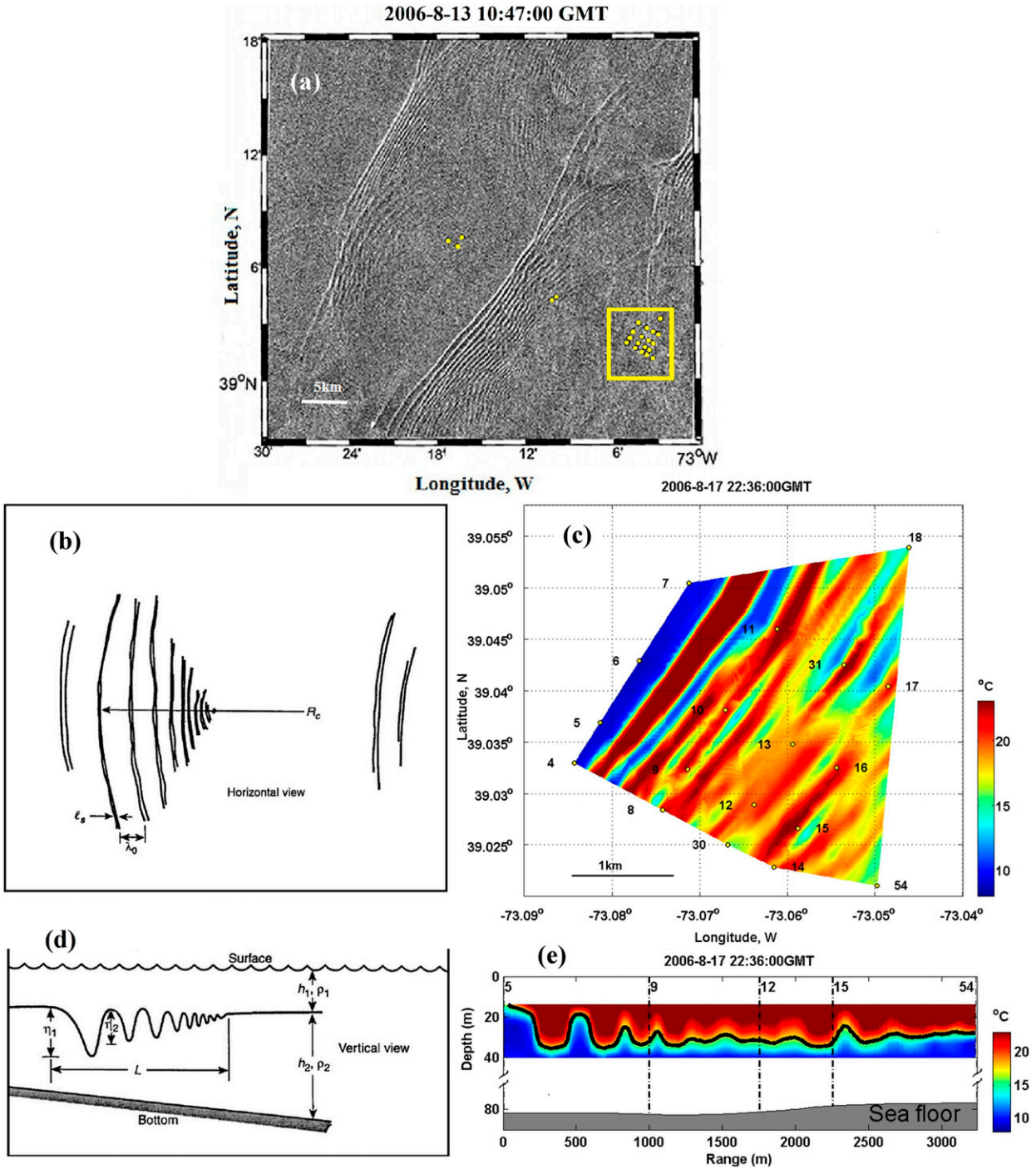


FIG. 1. (a) Satellite picture of IW packets on 13 Aug 2006 showing various wave front features. (b),(d) Schematic view of IWs in horizontal and vertical planes, respectively. (c),(e) IW observation in horizontal and vertical planes, respectively, during SW06. Panel (c) shows the enlarged map of the yellow box in (a) with interpolated temperature data (28.5 m below sea surface) within the thermistor farm at 2236:00 UTC 17 Aug 2006. The locations of thermistor farm containing 18 vertical arrays and their labels are represented by small yellow circular with black-numbered dots. Panel (e) shows the interpolated temperature profile between 14 and 40 m in the water column as a function of range during IW propagation through thermistors 54, 15, 12, 9, and 5. The black solid curve in (e) represents the temperature contour at 17°C, which was the temperature at the middle of the thermocline.

TABLE 1. IW characteristic parameters; d.u. = dimensionless unit; a. s. = across shelf.

| Characteristic (symbol) | Unit | Typical scale | SW06 results | Uncertainty |
|---|---|---|---|---|
| Upper layer depth ($H_1$) | m | 5–25 | 17.6 ± 3.7 | 2.4 |
| Lower layer depth ($H_2$) | m | 30–200 | 59.1 ± 3.7 | 2.4 |
| Direction ($\alpha$) | ° | a. s. | 309.8 ± 13.0,[a] 13.4 ± 8.7[b] | 0.2 |
| Wavelength ($\lambda_0$) | m | 100–1000 | 513.0 ± 179.8,[a] 1525.2[b] | 5.0 |
| First amplitude ($\eta_1$) | m | 0–30 | 4.9 ± 1.9,[a] 16.8 ± 3.6[b] | 2.4 |
| Second amplitude ($\eta_2$) | m | 0–30 | 4.5 ± 1.6,[a] 14.3 ± 4.9[b] | 2.4 |
| Soliton width ($L_s$) | m | 100 | 176.4 ± 58.8 | 5.0 |
| Number of solitons ($n$) | d.u. | 1–20 | 4.9 ± 1.7[a] | 2.2 |
| | | | 16.7 ± 4.3[b] | 4.1 |
| | | | 42.0 ± 2.8[c] | 6.5 |
| Speed ($v$) | m s$^{-1}$ | 0.5–1.0 | 0.8 ± 0.1 | 0.003 |
| Amplitude/upper depth ($\gamma$) | d.u. | 0–6 | 0.4 ± 0.2 | 0.1 |
| Slope of IW faces ($K$) | d.u. | 5–100 | 36.4 ± 24.4 | 19.0 |
| Packet length ($L$) | km | 1–10 | 5.5 ± 1.8,[a] 14.3 ± 2.0[b] | 0.02, 0.06 |
| Packet spacing ($D$) | km | 15–40 | 12.4 ± 5.8,[a] 34.4 ± 4.4[b] | 0.04, 0.11 |
| Decay constant ($\beta$) | km$^{-1}$ | 0.1–1.0 | 0.36 ± 0.33[d] | [d] |
| Radius of curvature ($R_c$) | km | 15 – ∞ | 4.2[d] | [d] |

[a] Group 1.
[b] Group 2.
[c] Group 3.
[d] Explanation in the text.

measured parameters and seven derived ones. To the extent possible, we have followed Apel's notation (Apel et al. 2007) in choosing these parameters. The mean value of each parameter, its standard deviation, and its estimated measurement error are listed in Table 1. The histograms of 13 parameters of the abovementioned set are shown in Fig. 4. The quantity $H_1$ is the depth of the warm surface layer using the contour of the temperature at the middle of the thermocline as the reference. The value of $H_2$, which is the depth of the cold bottom layer, is calculated from the difference between $H_1$ and the water depth at the thermistor farm (about 80 m). The mean value of $H_1$ for the 30 events is 17.6 m, and about 60% of the NLIW events vary between 12.5 and 17.5 m. Similarly, the value of $H_2$ is 59.1 m, and 47% of the total varies from 57.5 to 62.5 m. The NLIW propagation direction ($\alpha$) is the direction measured within the thermistor farm with respect to true north. Figure 4c shows that $\alpha$ is distributed into two groups. The average direction of the first group, which contains 90% of the NLIW events, is (309.8°) nearly perpendicular to the shelf-bottom isobath contours. For the second group, containing only 10% of the events, this direction is 13.4°, which is nearly parallel to the isobaths contour. These waves are likely radiating from the Hudson Canyon, rather than from the shelf break. The soliton wavelength ($\lambda_0$) here is the horizontal width between the troughs of the first two solitons. It is noticed that this parameter has two statistical groups. The wavelength of the second group (1525.2 m) is 3 times the value of the first group (513.0 m). In the first group, 40% of the results range from 375 to 525 m. The second group has only one event with a very different angle of approach (19.1°) and a much longer wavelength (1525.2 m) compared with the majority of other events in the data. The histograms of the first two soliton amplitudes—$\eta_1$ and $\eta_2$—are shown in Figs. 4e,f, respectively. Both $\eta_1$ and $\eta_2$ have two groups with the small amplitude group constituting 80% of these waves. The results in the large amplitude group (i.e., $\eta_1$: 16.8 m and $\eta_2$: 14.3 m) are about 3–4 times as large as the results in the small amplitude group (i.e., $\eta_1$: 4.9 m and $\eta_2$: 4.5 m). For 61% of these events, the value of $\eta_1$ is $>\eta_2$, hence the amplitude decay constant,

$$\beta = \frac{\ln(\eta_2/\eta_1)}{-\lambda_0} = 0.36\,\mathrm{km}^{-1} \qquad (1)$$

The parameter used to designate the NLIWs is their half-amplitude width. Defined in earlier studies, the half-amplitude width $L_s$ is a characteristic scale of soliton (Holloway 1987; Zheng et al. 1993) that can be used to define the profile of these nonlinear waves. According to our analysis shown in Fig. 4g, the half-amplitude width here is 176.4 m. For our study, the relationship between soliton wavelength and half-amplitude width can be expressed by $\lambda_0 \approx 2.91L_s$, whereas in Holloway (1987) it is $3.6L_s$. The number of solitons in a packet, $n$, is obtained by counting the observed solitons whose amplitude is larger than 1 m. The packet consists of three groups, shown in Fig. 4h. The first group constitutes about 73% of the total, $n = 4.9$, with a range between 2 and 8. The second group constitutes about 20% of the total events, $n = 16.7$, with a range between 10 and 21.

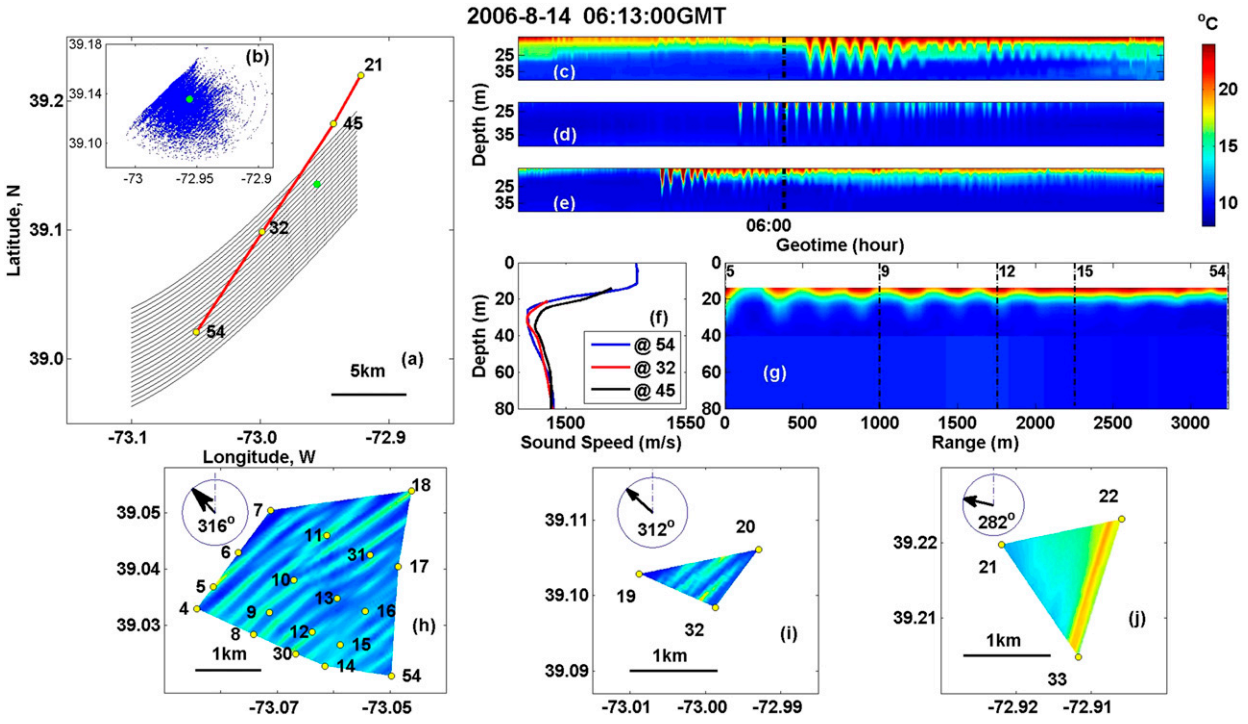


FIG. 2. This is a frame from the movie in the supplement showing the NLIW evolution from 0422:30 to 0650:30 UTC 14 Aug 2006. (a) IW fronts (i.e., gray curves) obtained by matching the IW propagation at three ocean patches [(h)–(j)] in the SW06 experimental area at 0613:00 UTC 14 Aug 2006. The numbered yellow dots show the locations of thermistor strings. The red line marks the reference track. (b) A ship radar image (blue dots) obtained by the R/V *Sharp* [position at the green dot in (a)]. (c)–(e) Time evolution of temperature profiles at positions 45, 32, and 54 along the reference track, respectively. The vertical black dashed–dotted lines indicate the reference time of this figure, 0613:00 UTC 14 Aug 2006. (f) The sound speed as a function of depth at thermistor 54 (blue), 32 (red), and 45 (black). (g) A side view of the interpolated temperature field along the track connecting the thermistor chains 54, 15, 12, 9, and 5. (h)–(j) Interpolated temperature data (24 m below sea surface) obtained by a three-dimensional mapping technique of evolving IWs at three ocean patches. The arrows represent the directions of IW propagation with respect to true north. The link for Movie 1 is http://dx.doi.org/10.1175/JTECH-D-15-0221.s1.

And finally, the third group has two events ($n$ = 40 and 44, respectively); their leading solitons have the largest amplitudes among the 30 events. If the largest amplitudes are caused by the combination of two closely neighboring packets, then the leading soliton of each of the two packets will have to be in phase and time aligned, which is not likely to occur. Therefore, the large number of solitons (i.e., $n \geq 40$) and the large leading soliton amplitudes for the two events in the third group are most likely from a single packet. The number of solitons in a packet can be used to estimate the lower-layer depth of the NLIW-generation source (Zheng et al. 1993). In the two-layer NLIW model,

$$n \leq 1 + \sqrt{\frac{32}{3} \times \frac{(H_1/H_2)[1-(H_1/H_2)]}{(\eta_1/H_1)}} \times \ln\left(\frac{6}{\pi}\frac{\eta_1}{H_1}\frac{H_{2S}}{H_1}\right), \quad (2)$$

where $H_{2S}$ is the lower-layer depth of the NLIW-generation source (Djordjevic and Redekopp 1978). The quantity $H_{2S}$ is the only unknown parameter in Eq. (1). Substituting the measured values into this equation, we obtain the lower-layer depth of the NLIW-generation source for the three groups. The values of $H_{2S}$ in the three groups are 198.8, $2.5 \times 10^5$, and $3.0 \times 10^{11}$ m, respectively. The result of the first group corresponds to the upper edge of the continental shelf break in this area (Zheng et al. 1993), indicating that perhaps the soliton packets in this group could be generated by the sharp change of the bottom tomography. The results

TABLE 2. Location of sensors deployed along the reference track in Fig. 2.

| Latitude | Longitude | Sensor number |
|---|---|---|
| 39°12.2900′ | −72°54.7050′ | 21, 22, **33** |
| 39°10.9574′ | −72°56.5750′ | 44, **45**, 46 |
| 39°05.9040′ | −72°59.9220′ | 19, 20, **32** |
| 39°01.2627′ | −73°02.9887′ | 14, 30, 8, 4, **54**, 15, 12, 9,5, 16, 13, 10, 6, 17, 31, 11, 7, 18 |

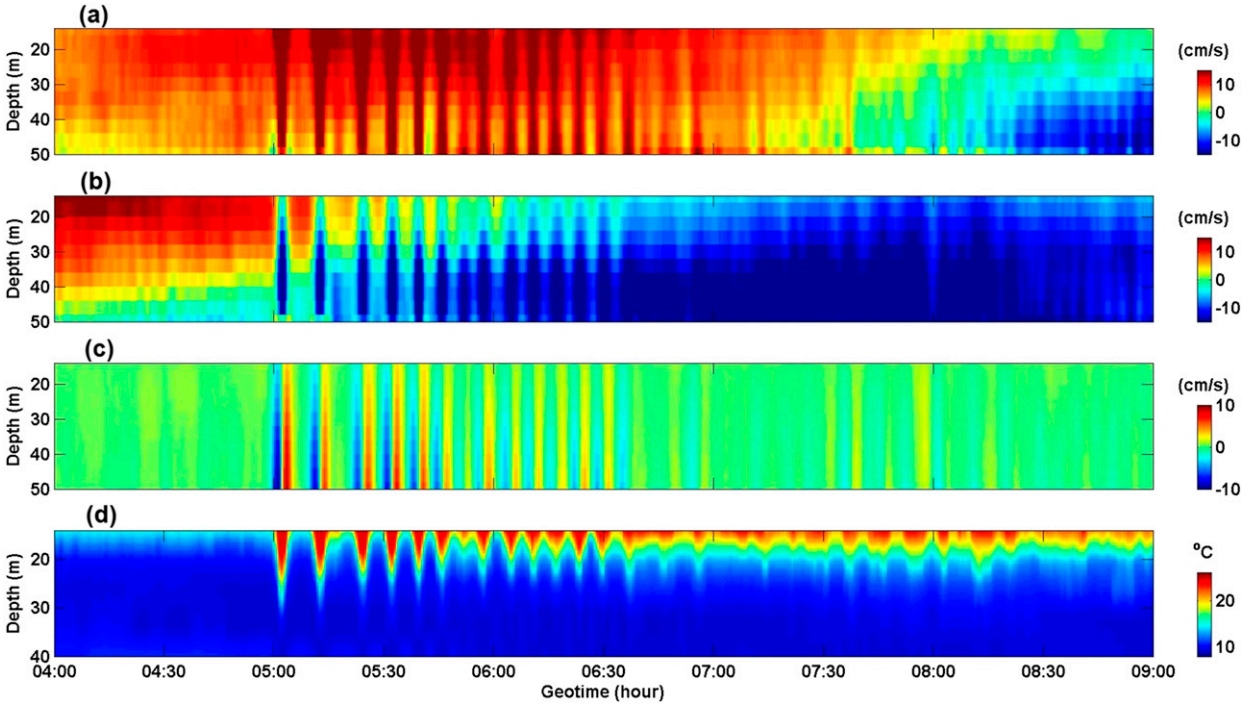


FIG. 3. (a) East–west component of the current speed at point 30 during an NLIW event on 14 Aug 2006, (b) north–south component, and (c) up–down (vertical) component, and (d) temperature profile measured at point 30 for the same time period.

of the second and third groups are not reasonable, because the soliton packets in these two groups are generated by different mechanisms, and Eq. (2) is not applicable here. The NLIW speed in this paper is referred to as the speed of the leading soliton of the internal wave packet in each event. Assuming the NLIW speed within the thermistor farm is constant, we have calculated the NLIW speed based on the propagation distance between the two farthest-apart thermistor chains (i.e., points 54 and 7 for the event shown in Fig. 1c) and the corresponding travel time, which is the arrival time difference of the leading soliton at these thermistor chains. The resulting average propagation speed is $0.8\,\mathrm{m\,s^{-1}}$, falling into the range of its typical scale shown in Table 1. The soliton amplitude to the upper-layer depth ratio ($\gamma = \eta_1/H_1$) determines the applicability of different NLIW models (Xu et al. 2010, 2011). As shown in Fig. 4j, the mean value of $\gamma$ for the 30 events is 0.4 and about 87% of the NLIW events vary between 0.1 and 0.7. We next look at the slope of NLIW faces (designated as $K$ here). In this paper, we define $K = L_s/\eta_1 = 36.4$. Its histogram is shown in Fig. 4k. Using the measured NLIW propagation speed ($v$), the packet length ($L$) and the spacing between the packets ($D$) can be estimated by

$$L(i) = [T_n(i) - T_1(i)] \times v(i) \tag{3}$$

$$D(i) = [T_1(i+1) - T_1(i)] \times v(i), \tag{4}$$

where $T_1(i)$ and $T_n(i)$ are the times when the first and last soliton of the $i$th NLIW packet arrive at the thermistor farm, respectively. The calculated results are shown in Figs. 4l,m. In Fig. 4l, the events in the second group have long packet lengths (i.e., 14.3 km) because of their large soliton numbers (i.e., $n \geq 40$ in Fig. 4h). The NLIW front curvature is of great importance for studying the NLIW. Using the satellite images obtained during SW06, the dominant value of the radius of curvature $R_c$ has been reported to be about 20–25 km (Lynch et al. 2010). In this paper we recognized only four NLIW events exhibiting obvious curved fronts within the thermistor farm area. Other events with a radius larger than 10 km exhibit almost straight NLIW fronts in this 4 km × 4 km area. The average value of $R_c$ in the four events is 4.2 km. It is noted that the statistical results of five parameters—that is, $\eta_1$, $L_s$, $v$, $\gamma$, and $K$—are obtained by using only the first soliton.

In describing the aforementioned statistics, we next consider the accuracy of the measurements, that is, the error in measuring these values. One source of measurement error is likely due to the array element's spatial and temporal resolutions and their spatial movement during the experiment (i.e., mooring motion); that is to say, the accuracy of a particular parameter value would depend on the spatial position (in 3D) of the array farm in

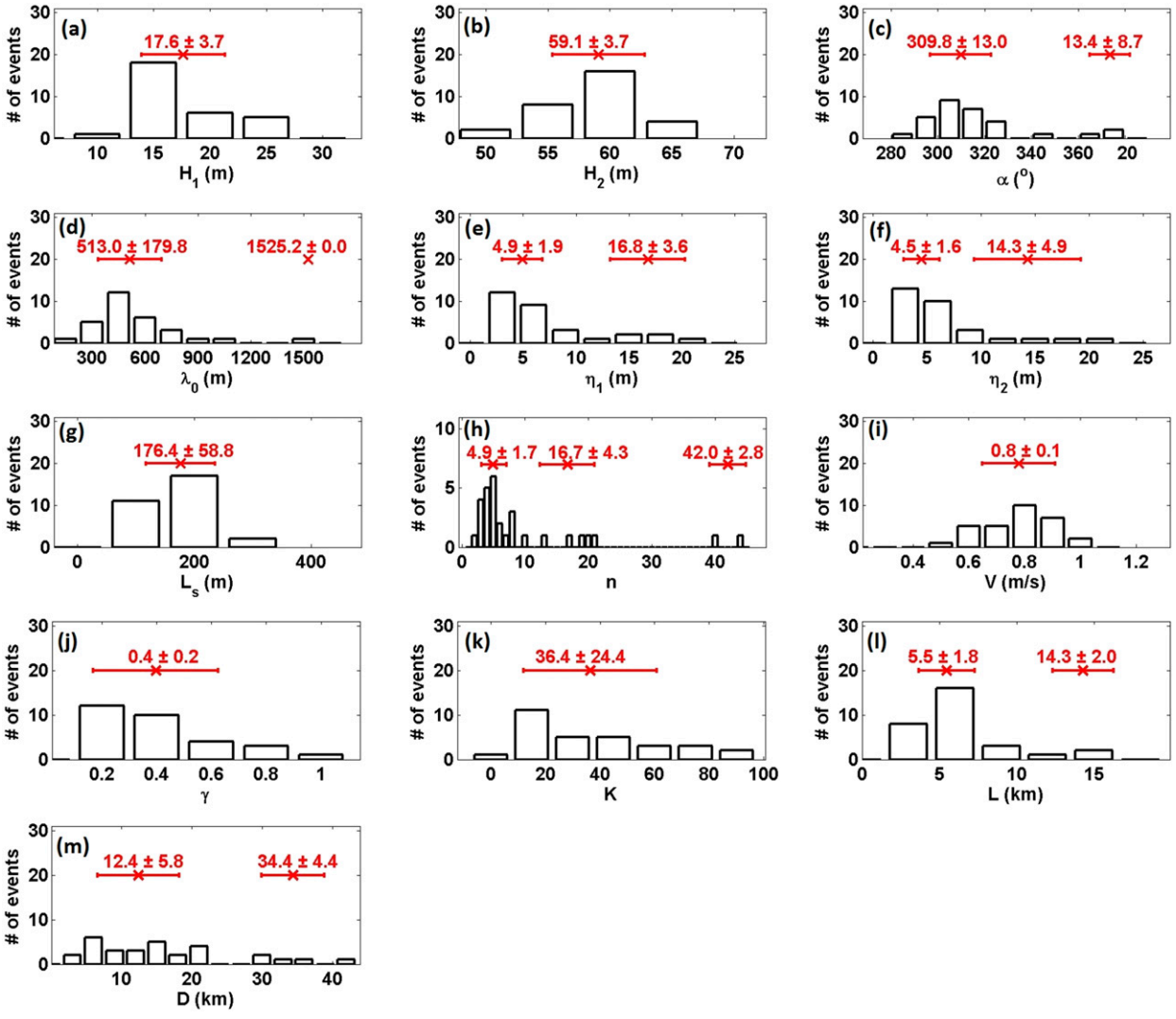


FIG. 4. Histograms of (a) $H_1$, (b) $H_2$, (c) $\alpha$, (d) $\lambda_0$, (e) $\eta_1$, (f) $\eta_2$, (g) $L_s$; (h) $n$, (i) $v$, (j) $\gamma$, (k) $K$, (l) $L$, and (m) $D$.

geotime. To assess this error in measurement, we assume that all the vertical arrays in the farm would move the same as the thermistor array installed on the so-called shark array (i.e., point 54). We know that each thermistor mooring is equipped with a pressure sensor, giving the value of the sensor array tilt and its elevation. At the shark array location, the movement of the array is accurately measured by an acoustic long baseline array navigation system. We will take the position of the shark array and assume that all 18 arrays in the farm during a given geotime behave in the same spatial and temporal manner. The maximum horizontal deviation of the shark's top sensor is about 5 m. The maximum vertical deviation is about 1.2 m (Newhall et al. 2007). Six temperature sensors, covering most of the thermocline, were deployed at depths of 13.3, 15.1, 18.8, 22.6, 26.3, and 33.8 m, respectively. The mean vertical spacing is 4.1 m. Thus, the uncertainty due to the vertical resolution of the temperature sensors is half of the vertical element spacing, that is, 2.1 m. The temporal error is assumed be due to the thermistor sampling intervals (30 s). The maximum error in sampling temperature is 15 s. All the measurements during the passage of the NLIW are made using the same spatial and temporal variations. The uncertainties of the 12 parameters coming from the array element's vertical resolution (2.1 m), temporal resolution (15 s), and their spatial movement (1.2 m in the vertical plane and 5.0 m in the horizontal plane) are obtained following Taylor (1997). The uncertainty of the number of solitons in a packet is estimated by applying Poison statistics; that is, the uncertainty is comparable to the square root of the number (Cowan 2011). All the calculated uncertainties are listed in the last column of Table 1.

## 4. Summary

From the results shown in Fig. 4 and Table 1, the following conclusions can be made: 1) the majority of the 30 NLIW events studied in this paper have the depth of the warm layer ($H_1$ = 17.6 m) and depth of the cold layer ($H_2$ = 59.1 m). 2) About 90% of the NLIWs propagate in the direction of 310° with respect to true north and originate near the New Jersey shelf break. About 10% of the NLIWs propagate at approximately 10°–13° with respect to true north and likely originate from the Hudson Canyon. The propagation speed of these waves (in both groups) is about 0.8 m s$^{-1}$. 3) The first and second soliton amplitudes in each packet during 61% of the total events indicate an amplitude decay of 0.36 km$^{-1}$. In some odd cases, the amplitude of the second soliton is larger than the first soliton, a peculiarity seen due to the variability in the background ocean affecting a nonlinear system. 4) The ratio of the soliton wavelength to the soliton width is about 2.91, this is comparable to the predicted ratio (Holloway 1987). 5) The average amplitude of the first soliton to the upper-layer depth ratio is 0.4. 6) The slope of the first soliton for the majority of the events in our database is about 36.4.

*Acknowledgments.* This research was supported by the Office of Naval Research Ocean Acoustics Program (322OA) through Grants N00014-10-1-0396 and N00014-11-1-0701. The authors are grateful to all the participants in SW06.

REFERENCES

Apel, J., L. Ostrovsky, Y. Stepanyants, and J. F. Lynch, 2007: Internal solitons in the ocean and their effect on underwater sound. *J. Acoust. Soc. Amer.*, **121**, 695–722, doi:10.1121/1.2395914.

Badiey, M., L. Wan, and A. J. Song, 2013: Three-dimensional mapping of evolving internal waves during the Shallow Water 2006 experiment. *J. Acoust. Soc. Amer.*, **134**, EL7–EL13, doi:10.1121/1.4804945.

Cowan, G., 2011: Recommendations for presentation of error bars. Preprints, *ATLAS Statistics Forum*, Meyrin, Switzerland, European Organization for Nuclear Research, 6 pp. [Available online at http://www.pp.rhul.ac.uk/~cowan/atlas/ErrorBars.pdf.]

Djordjevic, V. D., and L. G. Redekopp, 1978: The fission and disintegration of internal solitary waves moving over two-dimensional topography. *J. Phys. Oceanogr.*, **8**, 1016–1024, doi:10.1175/1520-0485(1978)008<1016:TFADOI>2.0.CO;2.

Holloway, P. E., 1987: Internal hydraulic jumps and solitons at a shelf break region on the Australian North West Shelf. *J. Geophys. Res.*, **92**, 5405–5416, doi:10.1029/JC092iC05p05405.

Lynch, J. F., Y.-T. Lin, T. F. Duda, and A. E. Newhall, 2010: Acoustic ducting, reflection, refraction, and dispersion by curved nonlinear internal waves in shallow water. *IEEE J. Oceanic Eng.*, **35**, 12–27, doi:10.1109/JOE.2009.2038512.

Moum, J. N., and J. D. Nash, 2008: Seafloor pressure measurements of nonlinear internal waves. *J. Phys. Oceanogr.*, **38**, 481–491, doi:10.1175/2007JPO3736.1.

Newhall, A. E., and Coauthors, 2007: Acoustic and oceanographic observations and configuration information for the WHOI moorings from the SW06 experiment. Woods Hole Oceanographic Institution Tech. Rep. WHOI-2007-04, 119 pp., doi:10.1575/1912/1826.

Ramos, R. J., B. Lund, and H. C. Graber, 2009: Determination of internal wave properties from X-band radar observation. *IEEE J. Oceanic Eng.*, **36**, 1039–1047, doi:10.1016/j.oceaneng.2009.07.004.

Sawyer, C., 1983: Tidal phase of internal-wave generation. *J. Geophys. Res.*, **88**, 2642–2648, doi:10.1029/JC088iC04p02642.

Shroyer, E. L., J. N. Moum, and J. D. Nash, 2009: Observations of polarity reversal in shoaling nonlinear internal waves. *J. Phys. Oceanogr.*, **39**, 691–701, doi:10.1175/2008JPO3953.1.

——, ——, and ——, 2011: Nonlinear internal waves over New Jersey's continental shelf. *J. Geophys. Res.*, **116**, C02033, doi:10.1029/2010JC006332.

Taylor, J. R., 1997: *An Introduction to Error Analysis: The Study of Uncertainties in Physical Measurements*. 2nd ed. University Science Books, 327 pp.

Xu, Z., B. Yin, and Y. Hou, 2010: Highly nonlinear internal solitary waves over the continental shelf of the northwestern South China Sea. *Chin. J. Oceanol. Limnol.*, **28**, 1049–1054, doi:10.1007/s00343-010-9018-1.

——, ——, and ——, 2011: Response of internal solitary waves to tropical storm Washi in the northwestern South China Sea. *Ann. Geophys.*, **29**, 2181–2187, doi:10.5194/angeo-29-2181-2011.

Zheng, Q., X.-H. Yan, and V. Klemas, 1993: Statistical and dynamical analysis of internal waves on the continental shelf of the Middle Atlantic Bight from space shuttle photographs. *J. Geophys. Res.*, **98**, 8495–8504, doi:10.1029/92JC02955.